Increasing the accuracy of binary neutron star simulations with an improved vacuum treatment

Amit Poudel,[1] Wolfgang Tichy,[1] Bernd Brügmann,[2] and Tim Dietrich[3]
[1]Department of Physics, Florida Atlantic University, Boca Raton, Florida 33431, USA
[2]Theoretical Physics Institute, University of Jena, 07743 Jena, Germany
[3]Institute of Physics and Astronomy, University of Potsdam, 14476 Potsdam, Germany

(Received 18 September 2020; accepted 9 October 2020; published 6 November 2020)

Numerical-relativity simulations are essential for studying the last stages of the binary neutron star coalescence. Unfortunately, for stable simulations there is the need to add an artificial low-density atmosphere. Here we discuss a new framework in which we can effectively set the density surrounding the neutron stars to zero to ensure a more accurate simulation. We test our method with a number of single star test cases and for an equal-mass binary neutron star simulation. While the bulk motion of the system is not influenced, and hence there is no improvement with respect to the emitted gravitational-wave signal, we find that the new approach is superior with respect to mass conservation and it allows a much better tracking of outward moving material. This will allow a more accurate simulation of the ejected material and supports the interpretation of present and future multimessenger observations with more accurate numerical-relativity simulations.

DOI: 10.1103/PhysRevD.102.104014

I. INTRODUCTION

Binary neutron star (BNS) systems are a unique laboratory for answering some of the most interesting questions in modern physics. For example: What is the equation of state (EOS) of supranuclear dense matter [1–9]? What is the expansion rate of the Universe [10–14]? How have the heavy elements in the cosmos [15–19] been produced? And, is general relativity the correct theory for describing gravity [20–23]?

An investigation of the full BNS coalescence requires a detailed analysis and understanding of the merger process. Because of the strong gravitational fields and the high velocities of the stars just before merger, one has to solve Einstein's equations with all nonlinearities using full $(3+1)$D numerical-relativity simulations [24–26]. Thus, numerical relativity has consolidated its role for the interpretation of compact binary mergers and was used to study the BNS merger GW170817 [27] and its electromagnetic counterparts [28].

To enable stable simulations, state-of-the-art numerical-relativity simulations of neutron stars use an artificial atmosphere to model vacuum and near-vacuum conditions outside the stars, see, e.g., [26,29–31]. Starting with the initial data for neutron stars in vacuum, the standard method fills all the vacuum regions with a very low-density atmosphere (often with a cold equation of state). This atmosphere is not physical and is artificially added for numerical reasons. One reason for this approach is that for the matter evolution we use conserved matter variables, i.e., variables whose change inside a given cell volume is determined by fluxes across the cell surfaces. To compute these fluxes one has to use interpolation from the cell centers to cell interfaces. In low-density regions this interpolation can return matter densities or energies that lie outside what is physically reasonable or allowed. An artificial atmosphere cures these issues. However, even with an artificial atmosphere, some of the same problems can still occur. In addition, the atmosphere has to be tuned to avoid most of these problems, while at the same time kept tenuous enough to not unduly influence the simulation. One of the most sophisticated atmosphere implementations is explained in [32]. In this approach a positivity preserving limiter is used for the density. Yet even in this approach a low-density atmosphere is still needed. However, it has the advantage that the density of the atmosphere can be made much lower than in more straightforward approaches so that the effects of the artificial atmosphere can be reduced. There is also a new hydrodynamics approach that uses Hamilton-Jacobi methods [33], and thus its evolution equations take a different form. Thus far it has been only used for barotropic fluids and, interestingly for us, in its current formulation it also requires an artificial atmosphere.

Our goal here is to find a scheme that does not explicitly add such an atmosphere. We will first describe the ingredients that allow us to perform simulations that contain true vacuum. After this we discuss tests of our new scheme, where we evolve neutron stars with and without atmosphere.

Throughout this study, we use dimensionless units where $G = c = M_\odot = 1$. and adopt the signature $(-,+,+,+)$ for the 4-metric. Greek indices on tensors run from 0 to 3 and

latin indices from 1 to 3, with the standard summation convention for repeated indices. The following can be used to convert from dimensionless units to the International System of Units: time $1000 = 4.93$ ms, distance $1 = 1.47735$ km, energy $1 = 1.7872 \times 10^{47}$ J, and density $1 = 6.177413 \times 10^{17}$ g/cm^3

II. NUMERICAL METHOD

A. The BAM code

We perform our dynamical simulations with the BAM code [30,34–37], which uses the method of lines with Runge-Kutta time integrators and finite differences approximating spatial derivatives. A Courant-Friedrich-Lewy factor of 0.25 is employed for all runs (see [34,38]).

The numerical domain contains a mesh made of a hierarchy of cell-centered nested Cartesian boxes and consists of L refinement levels from $l = 0$ to $L - 1$. Each refinement level is made out of one or more equally spaced Cartesian grids with grid spacing h_l. There are n points per direction on each grid plus a certain number of buffer points on each side. The levels are refined in resolutions by a factor of 2 such that the grid spacing in level l is $h_l = h_0/2^l$, where h_0 is the grid spacing of the coarsest level. The coordinate extent of a grid at level $l \geq 0$ entirely contains grids at any level greater than or equal to $l + 1$. The moving box technique is used to dynamically move and adapt some of the mesh refinement levels during the time evolution. These moving refinement levels are used for the cases like BNS where the center of each star moves during the time evolution. All levels with $l > l_{\rm m}$ are moving refinement levels. This is implemented in such a way that the moving refinement levels always stay within the coarsest level. The number of points in one direction for moving level ($n_{\rm m}$) can be set to a different value than n. There are six buffer points per direction on each side of the refinement grid; cf. Refs. [34,39] for more information about the buffer points. For simplicity, we shall always quote grid sizes without buffer points. For the wave zone, a shell made up from six "cubed sphere" patches [40–42] can be added. This helps to improve the accuracy in gravitational-wave (GW) extraction and allows for the implementation of boundary conditions derived for spherical geometries; see, e.g., [43].

B. Spacetime and matter evolution

We employ the Z4c formulation of the Einstein equations [43–45] combined with the moving puncture gauge using the $1 + \log$-slicing condition [46] and the gamma-driver shift [47,48]. For our single star evolutions, Sommerfeld boundary conditions [49] are used. For binary neutron stars, we add spherical patches outside of the coarsest cubic box to allow the use of constraint-preserving boundary conditions [44].

We assume that the matter is properly described as a perfect fluid for which the stress-energy tensor is given by

$$T^{\mu\nu} = (e + P)u^\mu u^\nu + P g^{\mu\nu}, \tag{1}$$

with the energy density e, the pressure P, and the four-velocity u^μ. The total energy density is given by $e = \rho(1 + \epsilon)$, where ρ is the rest-mass energy density and ϵ is the specific internal energy. In many equations we also use the specific enthalpy given by

$$h \equiv 1 + \epsilon + P/\rho. \tag{2}$$

The matter equations follow from the conservation law for the energy-momentum tensor and the conservation law for the baryon number. Following [50] the equations governing the evolution of general relativistic fluids, can be written in first-order flux-conservative form

$$\partial_t \vec{q} + \partial_i \vec{f}^{(i)}(\vec{q}) = \vec{s}(\vec{q}), \tag{3}$$

with $\vec{q}$ denoting the conserved variables, $\vec{f}^{(i)}$ the fluxes, and $\vec{s}(\vec{q})$ the source terms. The conserved variables are rest-mass density (D), the momentum density (S_i), and internal energy (τ) as seen by Eulerian observers. The conserved variables are related to the original variables via

$$D = \rho W, \tag{4}$$

$$S_i = \rho h W^2 v_i, \tag{5}$$

$$\tau = \rho h W^2 - P - \rho W, \tag{6}$$

where v_i is the three-velocity and W the Lorentz factor of the fluid.

To close the evolution system, we have to specify an EOS for the fluid. We choose to employ a simple ideal-gas EOS in our single star evolutions. For the BNS evolutions we use a more realistic EOS that is a piecewise polytropic fit to the zero-temperature SLy EOS [51–53] plus an additional thermal ideal-gas contribution [54] with $\Gamma^{\rm hot} = 1.75$ [55].

C. Dealing with low-density or vacuum regions

1. Original implementation in BAM

NSs surrounded by vacuum are modeled in numerical-relativity simulations by using an artificial atmosphere, e.g., [30,56–58]. The artificial atmosphere outside of the stars is chosen as a fraction of the initial central density of the star as $\rho_{\rm atm} \equiv f_{\rm atm} \cdot \rho_c(t = 0)$. The atmosphere pressure and internal energy is computed by employing the zero-temperature part of the EOS. The fluid velocity within the atmosphere is set to zero. At the start of the simulation, the atmosphere is added before the first evolution step. During

the recovery of the primitive variables from the conservative variables, a point is set to atmosphere if the density is below the threshold $\rho_{\rm thr} \equiv f_{\rm thr}\rho_{\rm atm}$. In this article, we are using $f_{\rm atm} = 10^{-11}$ and $f_{\rm thr} = 10^2$ in all test cases.

2. A new vacuum treatment

Conservative to primitive conversion.—Unfortunately, in general there is no closed analytic expression for the primitive variables in terms of the conserved ones. We thus have to resort to a root finder. Within our new vacuum treatment, we use the following scheme. We square Eq. (5) and use the definition of the conservative variables to find

$$W^2 = \frac{(D+\tau+P^*)^2}{(D+\tau+P^*)^2 - S^2}. \tag{7}$$

Here P^* is an initial guess for the pressure and we have defined $S^2 = \gamma^{ij}S_iS_j$. Once $W(P^*)$ is known, we can solve Eqs. (4) and (6) for ρ and ϵ. We obtain

$$\rho(P^*) = \frac{D}{W(P^*)} \tag{8}$$

and

$$\epsilon(P^*) = \frac{\sqrt{(D+\tau+P^*)^2 - S^2} - W(P^*)P^*}{D} - 1. \tag{9}$$

Using a one-dimensional root finder, we adjust P^* until the EOS of the form $P = P(\rho,\epsilon)$ is satisfied. However, both $W(P^*)$ and $\epsilon(P^*)$ contain a square root of $(D+\tau+P^*)^2 - S^2$. Thus, we need $P^* > S - D - \tau$. Furthermore, we expect the pressure to be positive. Thus, we need a root finder that searches for the root P^* in the interval $[P_{\rm min}, \infty)$, where

$$P_{\rm min} = \min(0, S - D - \tau). \tag{10}$$

Our algorithm employs a Newton-Raphson scheme but falls back on bisection whenever the Newton step would bring us outside the allowed interval. In addition, we limit Eq. (9) to not violate the weak energy condition; i.e., whenever $\epsilon(P^*) \leq -1$, we set it to $-(1. - 10^{-10})$. In most cases we can then find a root and obtain a suitable P^*. In cases where this is not possible, we reset all variables to vacuum; i.e., we set

$$D = \tau = S_i = \rho = \epsilon = P = v_i = 0. \tag{11}$$

We also reset all variables to vacuum if we find that $D < 0$, since negative rest mass densities are nonphysical. We point out that similar checks are also present with artificial atmospheres, but with larger threshold values.

Reconstruction and fluxes.—The evolution equations for the conserved fluid variables are computed from fluxes at cell interfaces where we do not have grid points. In order to obtain these fluxes, we interpolate the quantities necessary for computing them at the cell interface locations. For the smooth gravitational fields such as α, β^i, and γ_{ij} we use a sixth-order Lagrangian interpolation, while for the potentially nonsmooth matter fields we use a fifth-order WENOZ interpolation for the primitive variables [36,59]. The interpolation results at each interface are constructed in two ways: once from data to the left (L) of the interface and one from data to the right (R) of the interface. For the primitive variables this results in $\rho_{L/R}$, $\epsilon_{L/R}$ and $Wv_{iL/R}$.[1] Interpolation can still lead to unphysical values on either side. If the determinant of γ_{ij} is less than or equal to zero, we set it to 1 and also set $\rho_{L/R} = \epsilon_{L/R} = 0$. Furthermore, if $\rho_L < 0$ we set $\rho_L = \epsilon_L = 0$, and if $\rho_R < 0$ we set $\rho_R = \epsilon_R = 0$. In order to obtain the pressure $P_{L/R}$ as well as the sound speed squared $c^2_{sL/R} = \frac{1}{h}\left(\frac{\partial P}{\partial \rho} + \frac{P}{\rho^2}\frac{\partial P}{\partial \epsilon}\right)_{L/R}$, we use the EOS. If $c_s^2 < 0$ or $c_s^2 > 1$, we set it to zero; we also set it to zero if $\rho = 0$ or $h = 0$. We use the thus interpolated and limited primitive variables to compute the conserved variables as well as the fluxes $\vec{f}_{L/R}$ at both interfaces. In addition, we compute the speeds $\vec{\lambda}_{L/R}$ of the characteristic variables on both sides using

$$\lambda_1 = \alpha\frac{v^n(1-c_s^2) + \sqrt{C^2}}{1 - v^2c_s^2} - \beta^n, \tag{12}$$

$$\lambda_2 = \alpha\frac{v^n(1-c_s^2) - \sqrt{C^2}}{1 - v^2c_s^2} - \beta^n, \tag{13}$$

$$\lambda_3 = \alpha v^n - \beta^n, \tag{14}$$

$$\lambda_4 = \alpha v^n - \beta^n, \tag{15}$$

$$\lambda_5 = \alpha v^n - \beta^n, \tag{16}$$

where $C^2 = c_s^2\{(1-v^2)[g^{nn}(1-v^2c_s^2) - v^nv^n(1-c_s^2)]\}$, $v^n = v^in_i$, and n_i is the normal to the interface. If $1 - v^2c_s^2 = 0$ or $C^2 < 0$, we simply set $\lambda_1 = \lambda_2 = 0$.

The final numerical flux $\vec{F}$ at the interface is then computed using a standard method such as the local Lax-Friedrichs (LLF) scheme where

$$\vec{F}_{\rm interface} = \frac{1}{2}[\vec{f}_R + \vec{f}_L - |\lambda|_{\rm max}(\vec{q}_R - \vec{q}_L)]. \tag{17}$$

Here $\vec{q}_{L/R}$ are the conserved variables on the left or right and $|\lambda|_{\rm max}$ is the characteristic speed with the largest magnitude. In fact, in the simulations presented in this

[1]Notice that we interpolate Wv_i and not v_i to avoid cases where the three-velocity is interpolated to a value above light speed.

paper we always use the LLF flux at low densities, while possibly using a higher-order flux at higher densities. In this case, the higher-order flux $\vec{F}^{\rm HO}_{\rm interface}$ is obtained by interpolating the characteristic variables from five neighboring points using the WENOZ scheme [36]. In some simulations labeled with HO we use this higher-order flux $\vec{F}^{\rm HO}_{\rm interface}$ above a certain density threshold (typically on the order of 1% of the maximum of ρ at the star center).

Matter removal.—We use a fourth-order Runge-Kutta scheme to evolve the conserved variables. Before we evaluate the right-hand side within each Runge-Kutta substep, we set the conserved variables to vacuum if one of the following two conditions is true: (1) if $D < 0$, or (2) if $D > fW\rho$ and $\alpha < 0.2$, where the factor f is usually chosen to be 100. The first condition is obvious and allows only positive matter density. The second case is used for matter removal inside black holes (BHs). Since we use the standard moving puncture gauges $1+\log$-lapse and gamma-driver shift [47,48,60], the BH horizon is located near the surface where $\alpha \sim 0.3$. Therefore, condition (2) is true only inside the horizon. We have observed that when matter accumulates near the BH center after a star collapses, D rises much faster than ρ, so Eq. (4) is violated. This happens because the BH center in this gauge is only very poorly resolved [61,62]. Condition (2) ensures that matter is removed whenever D becomes much larger than ρ. An alternative approach was described in [63], where matter is not removed but some of the eigenvalues and W are reset for regularity, which could be explored in future work.

III. SINGLE STAR SPACETIMES

To test our new implementation, we start by studying three different single star configurations:

(1) A stationary, static star ($\mathrm{TOV}_{\rm static}$ (Tolman-Oppenheimer-Volkoff)—Sec. III A).
(2) An unstable, migrating star ($\mathrm{TOV}_{\rm mig}$—Sec. III B).
(3) A perturbed, collapsing, uniformly rotating neutron star ($\mathrm{RNS}_{\rm col}$—Sec. III C).

Each test uses the LLF flux with primitive reconstruction [64–66], labeled as LLF, and the hybrid scheme employing characteristic reconstruction for large and primitive reconstruction for low densities (labeled as HOLLF). We employ four different resolutions denoted as Low, Mid, High, and Fine. Details about the physical setup and the grid parameters are given in Tables I and II, respectively. In order to assess the performance of the old "atmosphere" and the new "vacuum" method, we compare the central density, the total rest mass, and the Hamiltonian constraint during the evolution for all tests.

A. Stationary TOV simulations

In Fig. 1, we plot the relative central density $1-\frac{\rho_c(t)}{\rho_c(t=0)}$, the relative rest-mass change $|1-\frac{M_b(t)}{M_b(t=0)}|$, and the Hamiltonian constraint for all $\mathrm{TOV}_{\rm static}$ simulations. All quantities are extracted at level $l=4$ which is the finest level but also fully covers the entire star. The stars are evolved up to a time of 1000 $M_\odot$, i.e., 4.93 ms. Truncation errors trigger small-amplitude pulsations in the stars [56,67] that can be seen as oscillations in the relative central density. The central density oscillations are larger for the hybrid HOLLF method but decrease clearly with an

TABLE I. Parameters and properties of the single neutron star tests. We report the density at which we switch between primitive and characteristic reconstruction ($\rho_{\rm switch}$), threshold density, and atmosphere density for the artificial atmosphere ($\rho_{\rm thr}$ & $\rho_{\rm atm}$), EOS parameters Γ and K for the polytropic EOS ($p=K\rho^\Gamma$) to set up the initial data, and we employ symmetry to reduce computational costs. For completeness, we also present the gravitational mass M, the baryonic rest mass M_b, the initial central density ρ_c, the equatorial radius R_e, and the aspect ratio R_p/R_e.

Stars	$\mathrm{TOV}_{\rm static}$	$\mathrm{TOV}_{\rm mig}$	$\mathrm{RNS}_{\rm col}$
$\rho_{\rm switch}\times 10^{-5}$	1.28	7.83	3.12
$\rho_{\rm thr}\times 10^{-12}$	1.280	7.9934	3.1160
$\rho_{\rm atm}\times 10^{-14}$	1.280	7.9934	3.1160
Γ	2	2	2
K	100	100	99.5
Symmetry	Octant	Octant	Quadrant
M	1.400	1.448	1.861
M_b	1.506	1.535	2.044
$\rho_c\times 10^{-3}$	1.2800	7.9934	3.1160
R_e	8.126	4.268	9.652
R_p/R_e	1	1	0.65

TABLE II. The grid parameters for the single star configurations at all four resolutions are tabulated here. The atmosphere and vacuum treatments have the same parameters and thus are tabulated only once. L is the total number of boxes, n (n^{mv}) is the number of points in the fixed (moving) boxes, and h_0, h_{L-1} are the grid spacings in level $l=0, L-1$. The grid spacing in level l is $h_l = h_0/2^l$.

	Grid parameters					
Tests	Resolutions	L	n	n^{mv}	h_0	h_{L-1}
$\mathrm{TOV}_{\rm static}$	Low (L)	5	64	64	1.125	0.281
	Med (M)	5	96	96	0.750	0.188
	High (H)	5	128	128	0.563	0.141
	Fine (F)	5	160	160	0.450	0.113
$\mathrm{TOV}_{\rm mig}$	Low (L)	7	64	64	19.20	0.300
	Med (M)	7	96	96	12.80	0.200
	High (H)	7	128	128	9.600	0.150
	Fine (F)	7	160	160	7.680	0.120
$\mathrm{RNS}_{\rm col}$	Low (L)	9	64	28	18.00	0.070
	Med (M)	9	96	42	12.00	0.047
	High (H)	9	128	56	9.00	0.035
	Fine (F)	9	160	72	7.20	0.028

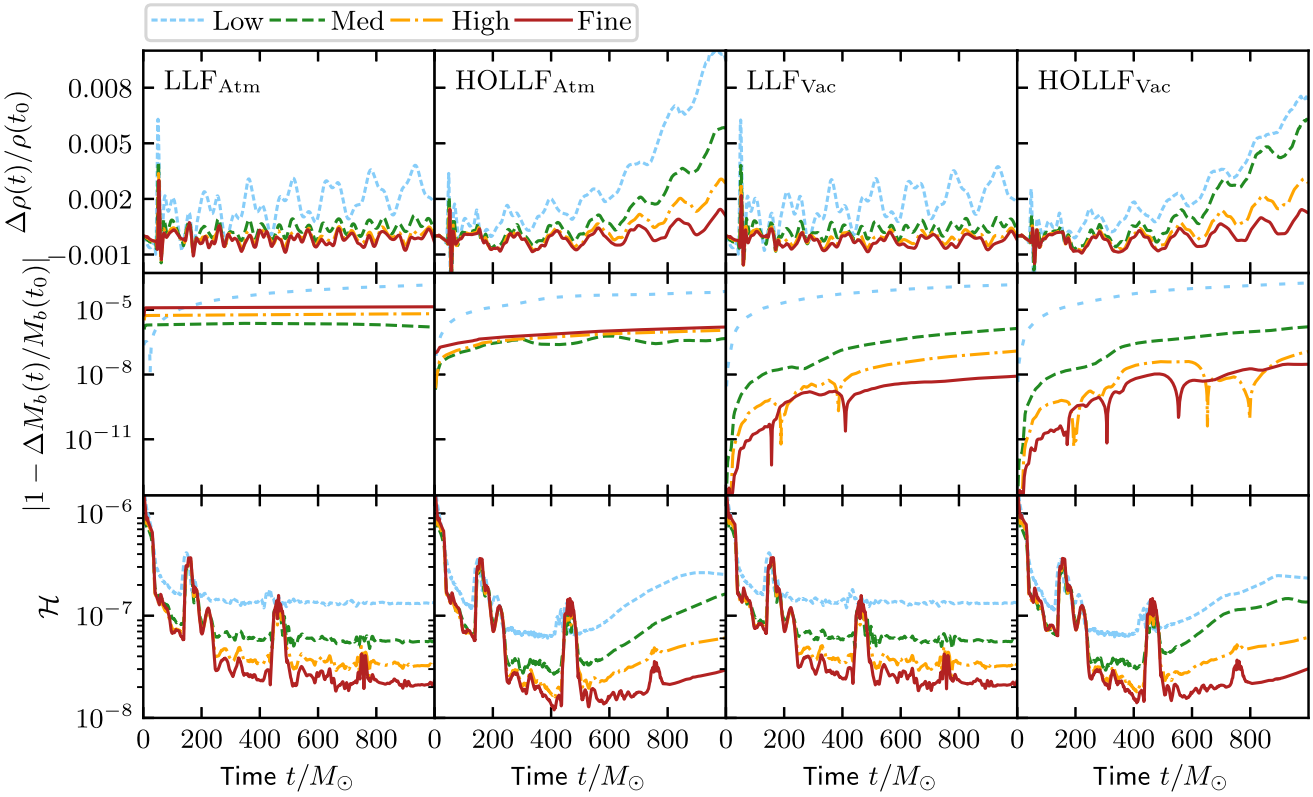

FIG. 1. Results of the TOV$_{\rm static}$ test. Left to right: Atmosphere-LLF, Atmosphere-HOLLF, Vacuum-LLF, and Vacuum-HOLLF. Top panels: relative change in central density $1-\frac{\rho_c(t)}{\rho_c(t=0)}$. Middle panels: relative rest-mass change $|1-\frac{M_b(t)}{M_b(t=0)}|$. Bottom panels: the time evolution of the Hamiltonian constraint ($\mathcal{H}$).

increasing resolution. There is no noticeable difference between the old atmosphere and the new vacuum method.

Considering the mass conservation, one sees a clear advantage of our new implementation. In the case of the old atmosphere method, the limit for setting the density to the atmosphere value is 1.28×10^{-12}. In the first few time steps, the star surface grows slightly, causing the density to drop below this threshold. This leads to a visible violation of mass conservation after the first time step. With our new vacuum approach a low-density layer builds up around the star. Thus, with our new approach mass is much better conserved. In addition, even during the subsequent evolution one observes a larger mass violation for the atmosphere method than for our new implementation, where for the highest resolution the mass violation is below 10^{-8}.

It is also important to point out that for the atmosphere case, we do not observe convergence in the mass. This applies to both the HOLLF and the LLF scheme. On the contrary, for the new vacuum method we find second-order convergence most of the time for LLF and up to $t=600\ M_\odot$ for HOLLF.

The bottom panel of Fig. 1 shows the evolution of the Hamiltonian constraint. We observe a reduction of the Hamiltonian constraint for increasing resolution exhibiting clean second-order convergence. As an example we show a convergence test for the LLF vacuum setup in Fig. 2. Here the differences in the Hamiltonian constraint are scaled by factors that correspond to assuming second-order convergence. These scaled lines nicely coincide with the middle line, as expected for second-order convergence.

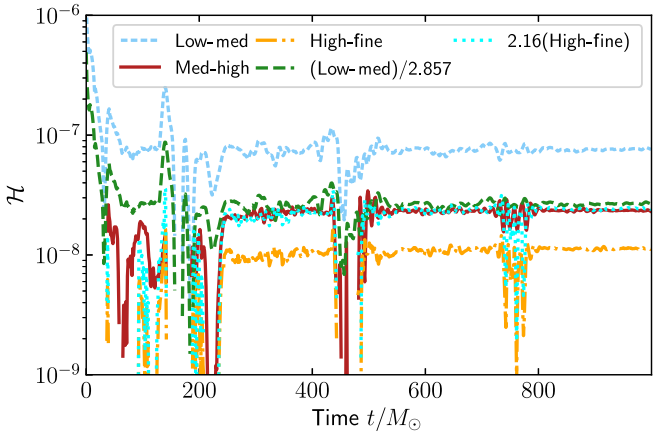

FIG. 2. Convergence test of the Hamiltonian constraint of the LLF vacuum case of a TOV$_{\rm static}$ neutron star. The dotted cyan and dashed green lines are obtained by scaling the dash-dotted orange line and the dashed blue line, respectively, in order to match up with the solid red line.

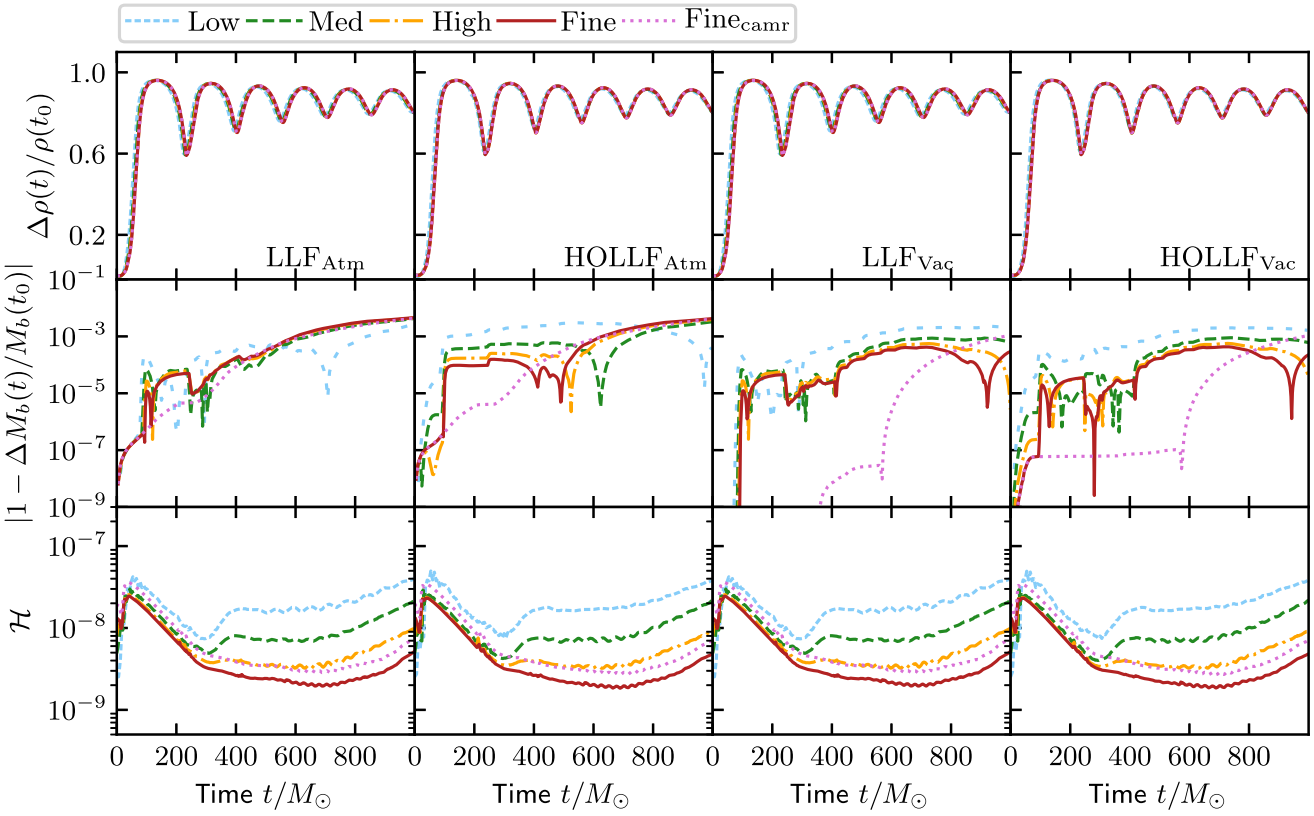

FIG. 3. Results of the TOV$_{\rm mig}$ test. Left to right: Atmosphere-LLF, Atmosphere-HOLLF, Vacuum-LLF, and Vacuum-HOLLF. Top panels: relative change in central density $1-\frac{\rho_c(t)}{\rho_c(t=0)}$. Middle panels: relative rest-mass change $|1-\frac{M_b(t)}{M_b(t=0)}|$. Bottom panels: the time evolution of Hamiltonian constraint ($\mathcal{H}$). Since matter is expected to cross refinement boundaries during this test, we also perform for the highest resolution a simulation in which we apply the conservative refluxing algorithm that we developed in [35].

B. Migration of an unstable star

TOV$_{\rm mig}$ represents a test based on the unstable U0 model of Ref. [30], with a central energy density of $\epsilon_c = 8.73 \times 10^{-3}$ and a gravitational mass of $M = 1.557$, A small perturbation caused by truncation errors leads to pulsations that migrate the star toward a stable configuration of the same rest mass. Initially, the central density decreases and the star expands rapidly. Later its inner core contracts, which leads to a shrinking of the star and an increase of the central density. As a result, it pulsates, causing matter to cross the grid refinement boundaries. To better resolve the dynamics, we are using a larger number of refinement levels than in the TOV$_{\rm static}$ test.

In Fig. 3 we plot the central density on the finest level $l = 6$ and the rest mass and Hamiltonian constraint on level $l = 1$. In the top panels, we see a decrease in the amplitude of pulsation of central density as the simulation progresses. If we would run the simulation longer, the star would finally settle down to a stable configuration. The Hamiltonian constraint in the bottom panels converges roughly with a second-order convergence in all four cases. For the LLF case we see convergence throughout the simulation, whereas in HOLLF we see convergence roughly from 300 to 1000 $M_\odot$. Thus, considering the Hamiltonian constraint, the LLF simulations perform better than the HOLLF ones.

As for the TOV$_{\rm static}$ case, we find a better mass conservation for the vacuum configurations than for the old atmosphere method. Convergence consistent with the second order is observed in the early part of the HOLLF simulations; for the LLF method no convergence at all is present. During the evolution time and because of the pulsation of the star, mass is crossing the refinement level. At this time, mass conservation is generally lost if no additional conservative refluxing step as introduced in [35,68] is applied. To prove this point, we perform a simulation with the highest resolution and activate the refluxing scheme, labeled as Fine$_{\rm camr}$ in Fig. 3. We find that for the vacuum method mass conservation is significantly improved up to about $t = 600\ M_\odot$. At this time low-density material hits the outer boundary of the considered computational domain and leaves it; consequently, the total mass cannot be conserved after this point.

Considering 2D snapshots of the matter evolution clearly reveals the advantage of the new vacuum treatment. As can be seen in Fig. 4, when very low-density material expands, it is stopped due to the artificial atmosphere (see the bottom left panel), while it expands freely in the vacuum case

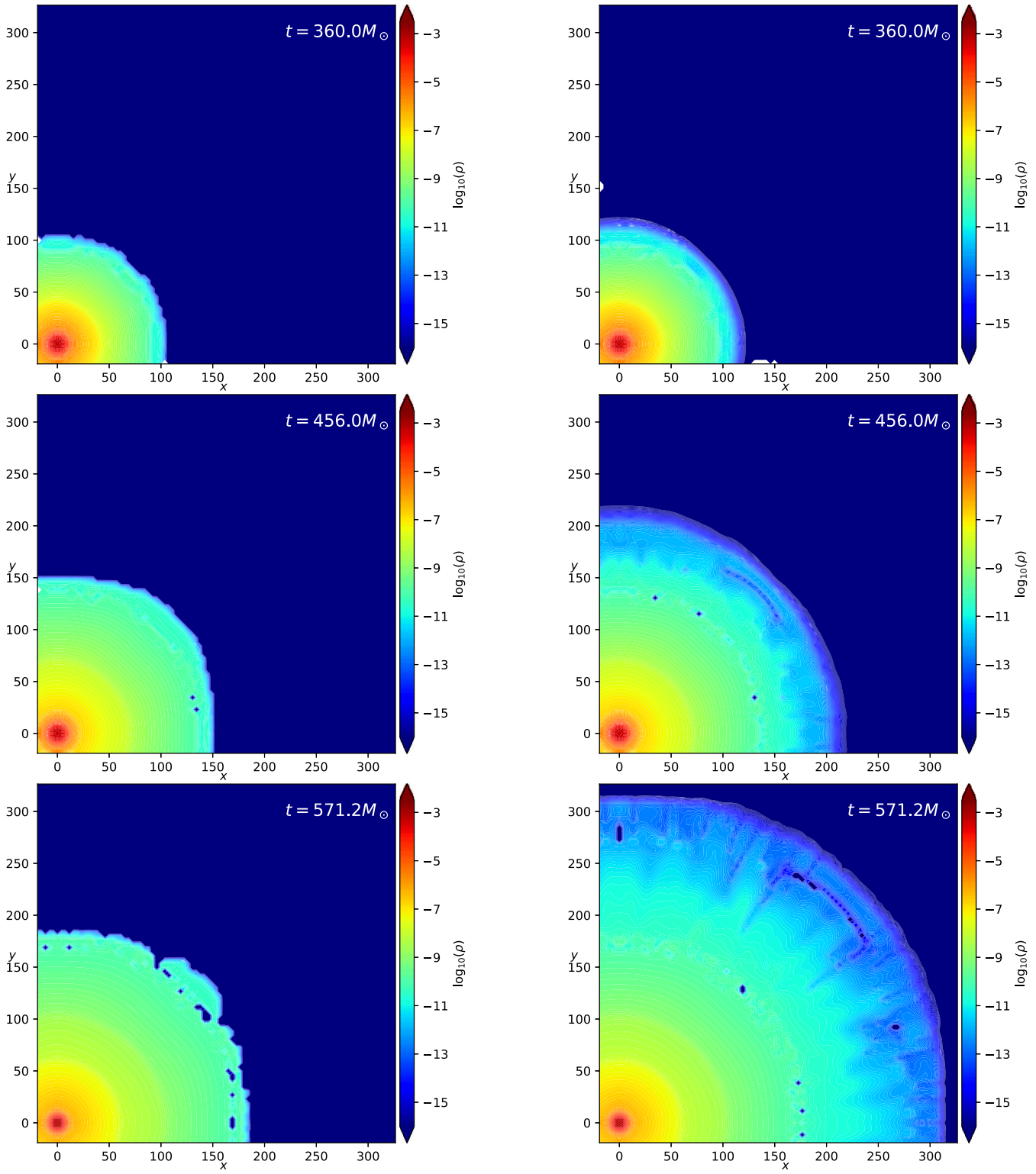

FIG. 4. The rest-mass density in the xy plane for the $\mathrm{TOV}_{\mathrm{mig}}$ test on refinement level $l = 1$ at different times for the finest resolution ($n = 160$ points) employing conservative mesh refinement [35]. The left panels show the previous atmosphere scheme, and the right panel shows the new vacuum implementation. For the atmosphere case, the threshold density below which artificial atmosphere is set up (ρ_{thr}) is $\sim 7.9934 \times 10^{-12}$ and the artificial atmosphere level (ρ_{atm}) is $\sim 7.993 \times 10^{-14}$.

(bottom right panel). Such an artificial impact on the outgoing matter could be of significant importance if one wants to track outward going ejecta.

C. Collapsing, rotating neutron star

As a last single-star test case, we study the collapse of a rotating neutron star (RNS). This test aims toward a better understanding if a BH can be properly modeled within our new algorithm.

The initial data are computed using a polytropic EOS with $K = 100$, $\rho_c = 3.1160 \times 10^{-3}$, and axis ratio 0.65, which leads to a star with gravitational mass of $M = 1.861$, baryonic mass of $M_b = 2.044$, and angular velocity of $\Omega = 3.96 \times 10^{-2}$. The star is evolved with the polytropic EOS with $K = 99.5$ and $\Gamma = 2$. This initial perturbation due to the change of the EOS triggers the collapse of the star to a BH. A similar configuration has been investigated in the past, e.g., Refs. [69–71]. We are evolving the star with quadrant symmetry, i.e., use reflection symmetry along the x and y axes, and employ nine refinement levels.

In Fig. 5 we plot the central density in the finest level $l = 8$ and the rest mass and Hamiltonian constraint on level $l = 3$. The collapse to a BH happens at around $t = 200\ M_\odot$ in most cases except for the lowest resolution using the LLF scheme. For both vacuum and atmosphere cases with LLF at $n = 64$ points, collapse happens at around $t = 380\ M_\odot$. After the star collapses into a BH, matter is removed to avoid the occurrence of steep density gradients, as mentioned before.

The Hamiltonian constraint shows second-order convergence before the BH formation. After the collapse, the convergence order reduces to first order. In both the vacuum and atmosphere cases, the error of rest mass behaves in a similar way.

Overall, we find no clear and noticeable difference between the old atmosphere and new vacuum method.

D. Summary of the single star simulations

We have studied evolutions with an updated implementation of our vacuum treatment for a number of single star spacetimes. The main observations are as follows:

(a) Mass conservation can be improved with the new implementation; cf. $\mathrm{TOV}_{\mathrm{static}}$.
(b) The new implementation improves the simulation of outflowing, low-density material; cf. $\mathrm{TOV}_{\mathrm{mig}}$.
(c) The new vacuum method is capable of tracking the BH formation; cf. $\mathrm{RNS}_{\mathrm{col}}$.

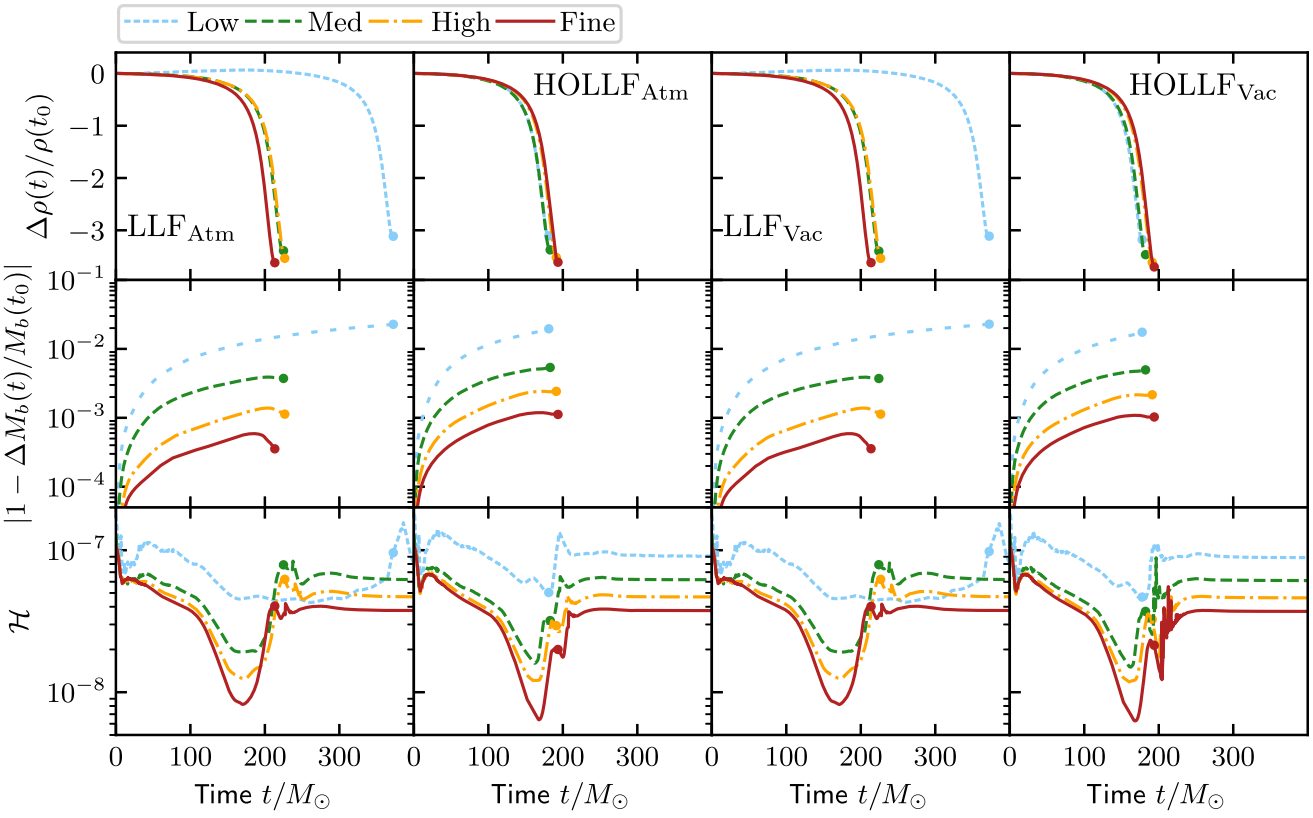

FIG. 5. Results of the $\mathrm{RNS}_{\mathrm{col}}$ test. Left to right: Atmosphere-LLF, Atmosphere-HOLLF, Vacuum-LLF, and Vacuum-HOLLF. Top panels: relative change in central density $1 - \frac{\rho_c(t)}{\rho_c(t=0)}$. Middle panels: relative rest-mass change $|1 - \frac{M_b(t)}{M_b(t=0)}|$. Bottom panels: the time evolution of the Hamiltonian constraint ($\mathcal{H}$).

IV. BINARY NEUTRON STAR EVOLUTIONS

A. Binary configurations

Finally, we want to discuss the performance of our new vacuum treatment for the simulation of BNS setups. We focus here on the simulation of an equal-mass, nonspinning configuration evolved with the old atmosphere and the new vacuum method. To save computational costs, we perform simulations only with the HOLLF scheme, for which Ref. [36] showed its superiority compared to the LLF scheme with primitive reconstruction.

The individual stars have a baryonic mass of 1.495 and a gravitational mass in isolation of 1.350. For the EOS, we use a piecewise polytropic fit of the zero-temperature SLy EOS [51–53] and add an additional thermal ideal-gas pressure component during the dynamical simulation.

The initial data are calculated using the pseudospectral SGRID code [72–74]. The initial separation of the stars is 35.5, i.e., 52.4 km, which results in an orbital frequency of 0.0070, an initial Arnowitt-Deser-Misner (ADM) mass of 2.678, and an initial ADM angular momentum of 7.686. The eccentricity of the inspiral is approximately 1.3×10^{-4}. This relatively low value has been achieved by using the eccentricity reduction discussed in [74].

Details about the grid setup for the BAM evolutions are given in Table III. To save computational costs, we have employed bitant symmetry. In contrast to the single star tests, we substitute a shell made up of six cubed sphere patches [40–42] for the outermost Cartesian box (level $l = 0$). In this shell matter is not evolved.

B. Dynamical evolution

During the inspiral, a general (almost linear) reduction of the central density is visible. This linear trend is reduced significantly with increasing resolution and is connected to the numerical dissipation [36], which decreases with decreasing grid spacing; cf. Fig. 6. Overall, there is generally a second-order convergence in the central density visible for both the atmosphere and the vacuum method.

In addition, we plot the time evolution for the central density for the two highest resolutions in Fig. 7. Clearly visible are large density oscillations after the merger, which correspond to radial oscillations of the formed hypermassive neutron star (HMNS); see, e.g., Refs. [77,78] for further details. The main difference between the old atmosphere and the new vacuum method is that for the two highest resolutions the lifetime of the HMNS is shorter for the vacuum method than for the atmosphere treatment. We note that the determination of the remnant's lifetime does influence (i) the material outflow and its composition and (ii) the properties of the BH + disk system, i.e., the potential short gamma-ray burst.

The middle panel of Fig. 6 shows the conservation of the rest-mass density, where we note that these simulations do not yet employ the conservative refluxing algorithm. We plan to repeat the simulations with conservative refluxing in the future when we have more computer time. The error of the rest mass seems to decrease as we go to higher resolutions. For the highest resolution, the total rest mass is conserved up to 0.5% throughout the inspiral, independent of the employed atmosphere/vacuum scheme. For the Hamiltonian constraint, convergence consistent with the second order is seen until 2000 $M_\odot$ in both the atmosphere and vacuum cases. After that, the order of the convergence rises up to fourth order, which is higher than theoretically expected. However, throughout the simulation there is a clear pattern of the Hamiltonian constraint decreasing for both cases as we go to higher resolutions. Looking at the plots of these three quantities, there is not a clear advantage for either the atmosphere or the vacuum method.

TABLE III. The grid parameters for the BNS simulations. The atmosphere and vacuum simulations use the same grid configurations to allow a proper comparison. L denotes the total number of levels, l^{mv} the finest nonmoving level, n (n^{mv}) the number of points in the fixed (moving) boxes, and h_0, h_{L-1} the grid spacings in levels $l = 0, L-1$. The grid spacing of level l is $h_l = h_0/2^l$. n_r is the radial point number, and n_θ is angular point number.

Resolutions	L	l^{mv}	n	n^{mv}	h_0	h_{L-1}	n_r	n_θ
Low	7	2	128	64	15.040	0.235	128	56
Med	7	2	192	96	10.027	0.157	192	84
High	7	2	256	128	7.520	0.117	256	112
Fine	7	2	320	160	6.016	0.094	320	140

C. Gravitational waveforms

For both methods an increasing resolution leads to a later merger, which is due to the increase of the numerical dissipation for lower resolutions. For the simulations with BAM code this effect is discussed in [36]. We report the merger time in Table IV for all BNS simulations. Most importantly, the difference between the atmosphere and vacuum methods decreases with increasing resolution; consequently, the two methods seem to lead to a similar continuum limit.

In Fig. 8, we present the GW signal for all simulations in the top panels for the atmosphere (left panels) and the vacuum methods (right panels). The bottom panels shows the phase differences between different resolutions. We rescale the phase differences assuming second-order convergence (dashed lines) and generally find that both methods show the expected convergence order, with a sightly better convergence behavior for the original atmosphere treatment. For all methods the low-resolution simulation stops being second-order convergent after about $1500M$, which indicates that this resolution is not sufficient to be in the convergent regime until merger. Overall, we find very close agreement between the individual phase differences reported in Fig. 8. In the bottom right panel, we show the phase difference between the two highest resolutions for the vacuum (solid, orange line) and the

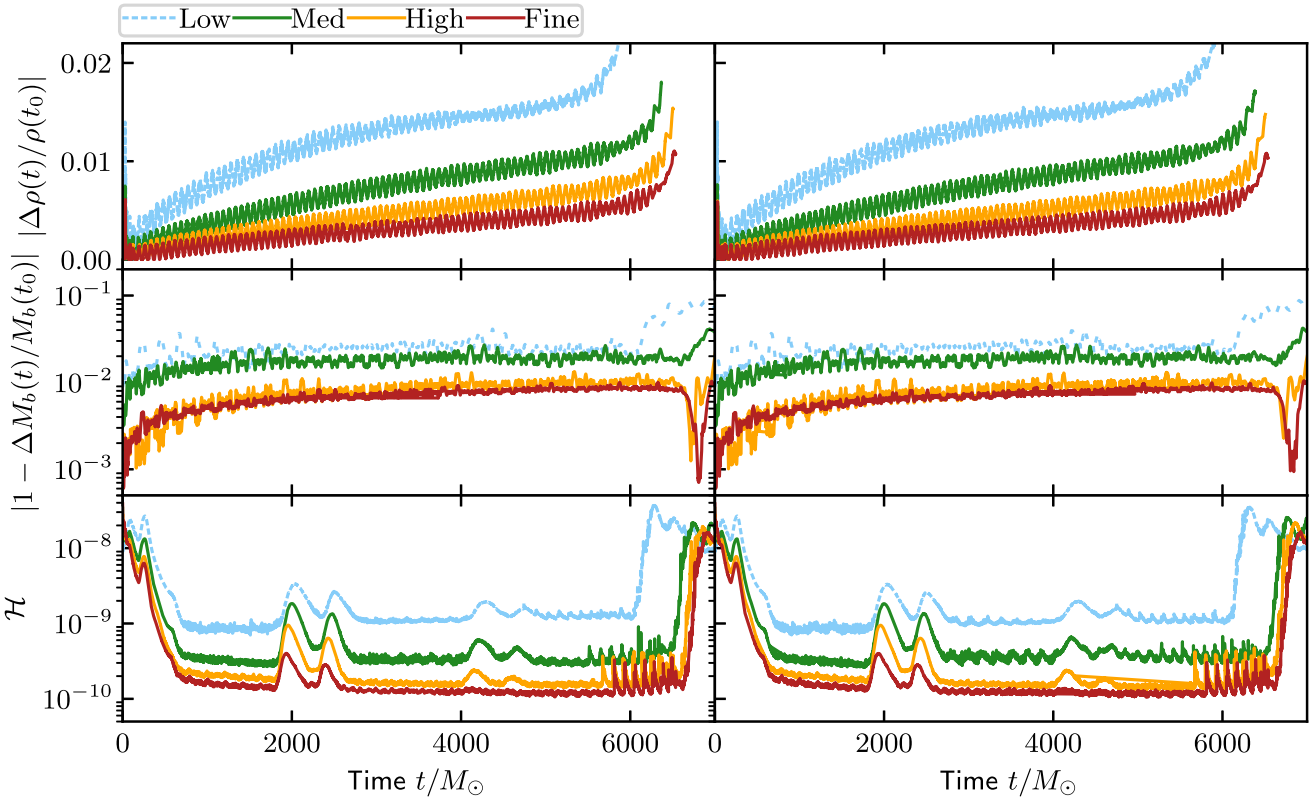

FIG. 6. Results of the BNS runs. Left to right: Atmosphere-HOLLF and Vacuum-HOLLF. Top panels: relative change in central density $1-\frac{\rho_c(t)}{\rho_c(t=0)}$. Middle panels: relative rest-mass change $|1-\frac{M_b(t)}{M_b(t=0)}|$. Bottom panels: the time evolution of Hamiltonian constraint ($\mathcal{H}$). We employ a Savitzky-Golay filter [75,76] to increase the visibility of the presented curves.

atmosphere method (purple, dotted line). We find that the difference is almost identical; thus, there is no improvement in the extracted GW signal for our new vacuum method, which we assume is because the overall bulk motion is dominating the GW radiation and the new vacuum treatment mostly affects the low-density regions.

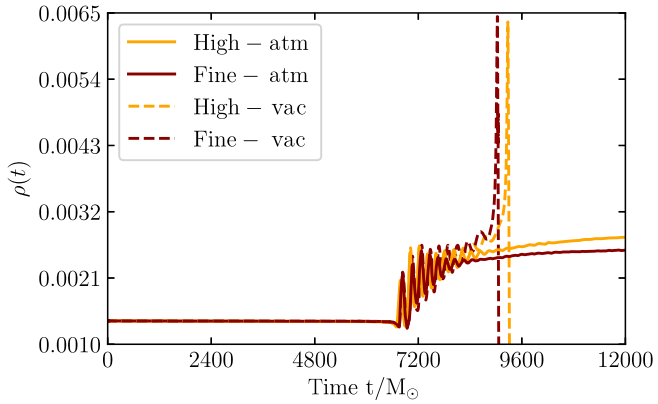

FIG. 7. Central density of the BNS for the simulations with the two highest resolutions. Solid lines are for the atmosphere and the dashed lines are for the vacuum methods. This plot shows how density changes in BNS during inspiral, merger, postmerger, and black hole formation.

D. Ejecta quantities

Since the amount of ejected material is tightly connected to the creation of electromagnetic counterparts for a BNS merger (see, e.g., Ref. [79] and references therein), it is important to improve the evolution of low-density material.

Generally, when material gets ejected, the fluid expands and the density reduces until it finally falls below the artificial atmosphere threshold used within the atmosphere implementation. In the atmosphere case such fluid elements are then set to atmosphere values with zero velocity, and they are thus no longer counted as ejecta so that the ejecta mass decreases. This trend is clearly visible in Fig. 9. The

TABLE IV. Merger times for atmosphere and vacuum cases at different resolutions. Here Low, Med, High, and Fine are simulations with resolutions 64, 96, 128, and 160 points respectively. The merger time values are in geometric units where 6000 $M_\odot \approx 30$ ms.

Tests	Low	Med	High	Fine
BNS atm	6117 $M_\odot$	6583 $M_\odot$	6682 $M_\odot$	6740 $M_\odot$
BNS vac	6150 $M_\odot$	6612 $M_\odot$	6689 $M_\odot$	6737 $M_\odot$

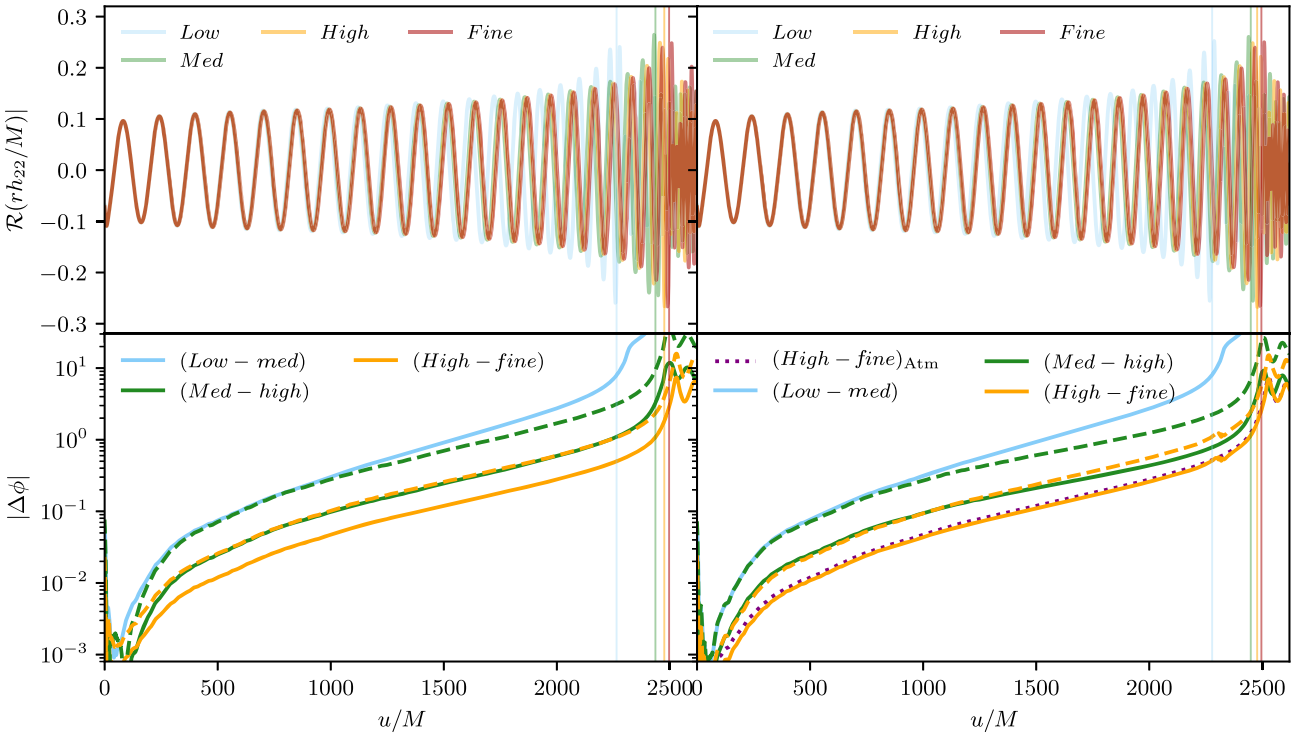

FIG. 8. In the top panels, we plotted the GW signal for both the old atmosphere method (left panel) and the new vacuum method (right panel). The bottom panels show the phase differences between different resolutions. The dashed lines are the rescaled phase differences assuming second-order convergence. The bottom right panel also includes the phase difference of the two highest resolutions for the atmosphere method for an easier comparison. Overall, we find similar phase difference and convergence properties for the methods.

problem is present mostly at the outer region of the ejected material for material which moves with the highest velocities. Consequently, removing this material also leads to a drop in $v_{\rm ej}$ for the atmosphere simulations.

We have made 2D plots to further investigate the difference in mass ejection in the atmosphere and the vacuum methods (see Figs. 10 and 11). We plot the mass density, velocity, and ejecta mass density at level $l = 1$ of the finest resolution simulation. We use a linear (velocity) as well as logarithmic (mass density and ejecta mass density) color scales and plot two snapshots in time at 1 (Fig. 10) and 11 ms (Fig. 11) after the merger. We choose these two times for the following reasons. Both methods begin with identical ejecta, the same velocity, and similar mass density. As the ejecta expand to a larger radius the density in the outer regions of the ejecta mass drop below the atmosphere threshold value. Thus, low-density material is removed and the ejected matter never reaches the outer boundary. Therefore, we find that the outflowing material seems to stall about ∼10 ms after the merger at a maximum radial extend of ∼350. In the vacuum case, the ejecta moves farther out. The eventual mass reduction for the vacuum method in Fig. 9 at late times can be explained by unbound material reaching the boundary of level 1, which is the outermost refinement level where matter is evolved. We also note that we see in the bottom right panel of Fig. 10 a clear imprint of the refinement boundaries on the low-density material. We expect, as in the $\rm TOV_{mig}$ case, that the use of the conservative refluxing algorithm would resolve this issue but postpone this test due to the high computational costs of the presented BNS simulations.

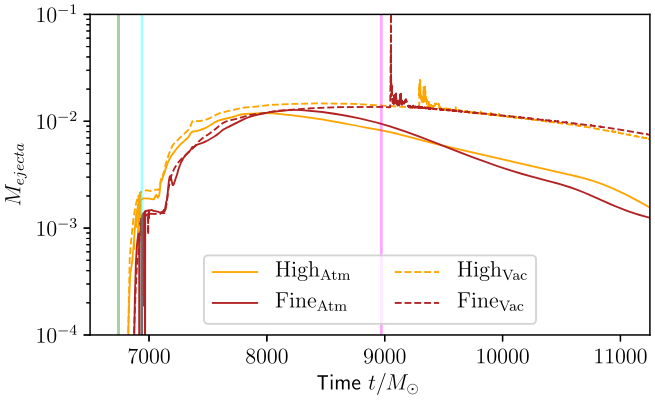

FIG. 9. The ejecta mass for the two highest resolutions. The vertical lines indicate the merger time, the time 1 ms after the merger, and the time 11 ms after the merger. For the last two, 2D plots are shown in Figs. 10 and 11. The spike in the vacuum simulations occurs due to the formation of the BH.

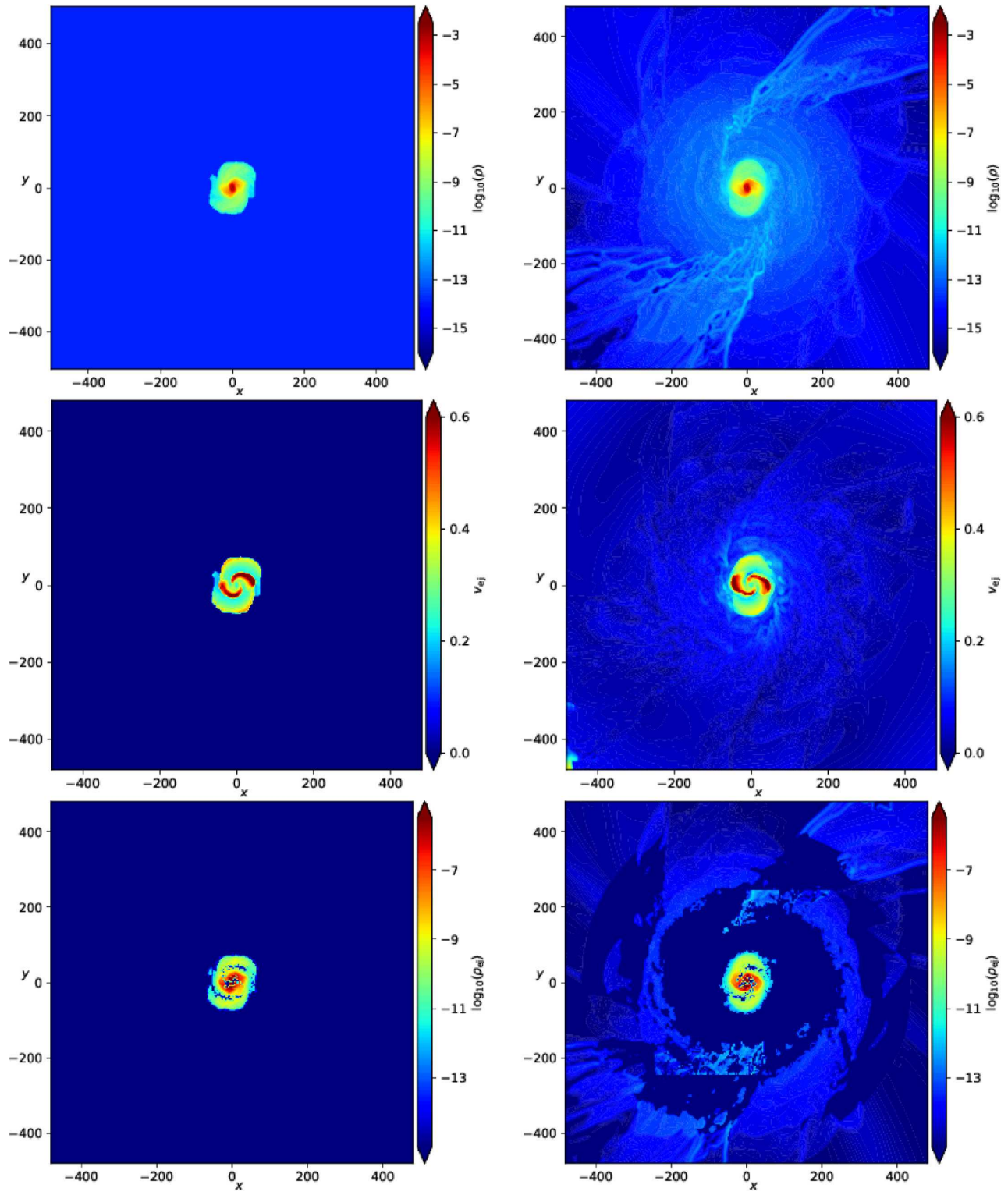

FIG. 10. Snapshots of the mass density (top panels), velocity (middle panels), and ejecta mass density (bottom panels) in the xy plane of BNS simulation at 1 ms after merger (vertical cyan line in Fig. 9). The finest resolution for both the atmosphere (left panels) and the vacuum (right panels) is plotted with linear (for velocity) and logarithmic color scales (for mass density and ejecta mass density). This is on level $l = 1$, which extends up to 481.28. The atmosphere threshold density is $\rho_{\rm thr} = 1.389 \times 10^{-12}$. We label material as unbound in case the fluid's 0th component of the four-velocity is smaller than 1 ($u_t < -1$) and the three-velocity is radially outward pointing.

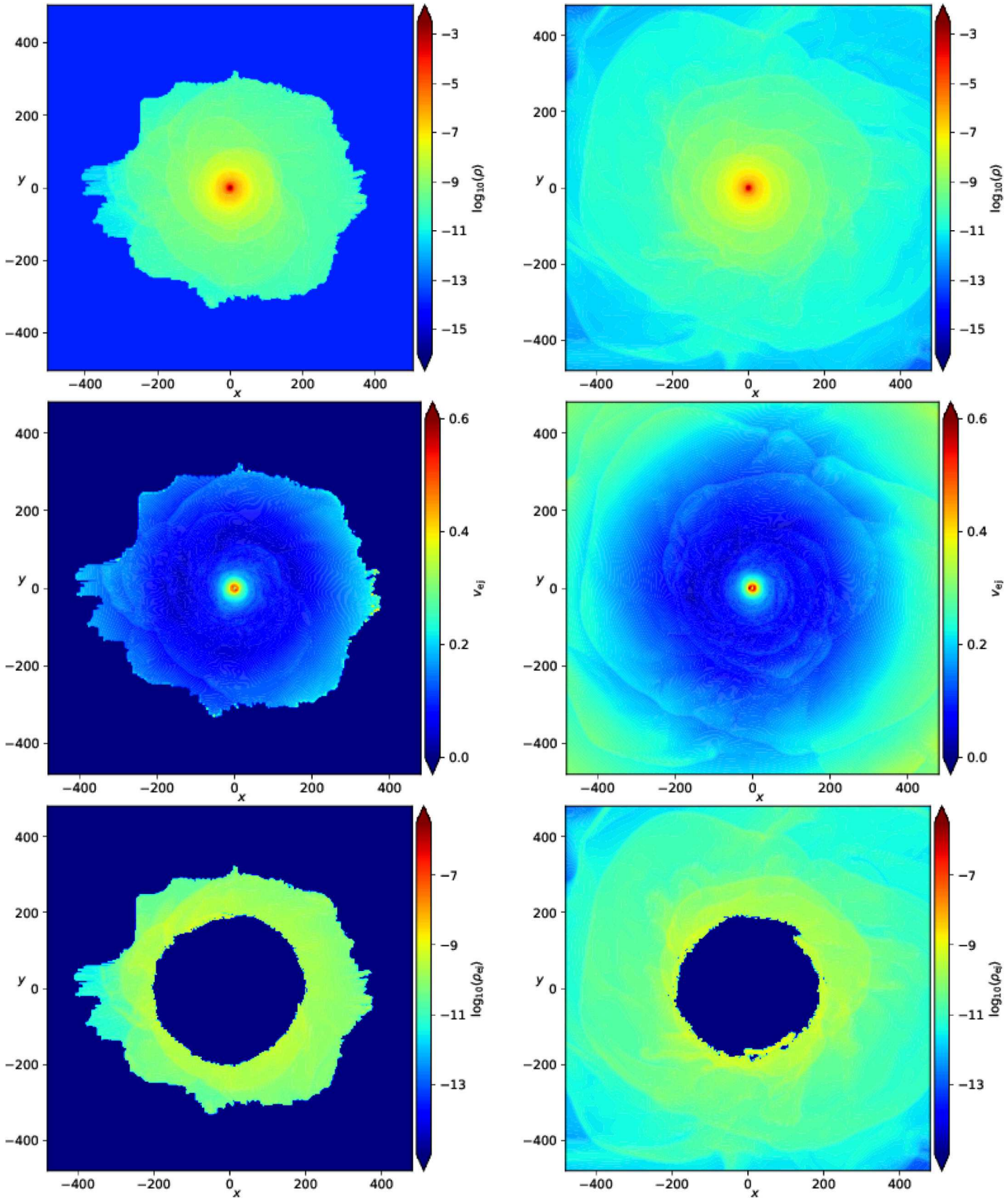

FIG. 11. Snapshots of the mass density (top panels), velocity (middle panels), and ejecta mass density (bottom panels) in the *xy* plane of the BNS simulation. The finest resolution for both the atmosphere (left panels) and the vacuum (right panels) at 11 ms after the merger (vertical cyan line in Fig. 9) is plotted with a linear (velocity) and logarithmic (mass density and ejecta mass density) color scales.

V. CONCLUSION

In this article, we have introduced and studied a new method to improve the vacuum treatment for general relativistic hydrodynamics simulations. Our recipe allows us to not set an explicit atmosphere value on the outside of a star, which improves the quality of our simulations. Previously, we implemented a method in BAM code that used an artificial atmosphere while recovering primitive variables. We have extensively tested both methods (vacuum and atmosphere) in single star spacetimes focusing on their performance when combined with a second-order local Lax-Friedrich and higher-order numerical flux schemes. The use of vacuum methods shows improvement in the mass conservation throughout our simulations. Typically, for the star that forms a low-density region during evolution, the mass conservation drops in the atmosphere method. Up to 0.5% mass loss was detected in the atmosphere method when the low-density layer crosses the refinement boundary. The violation of mass conservation at the grid refinement boundary does not occur in the case of our improved vacuum method. In most cases, the vacuum method leads to second-order convergence of the mass, in contrast to the atmosphere case, where second-order convergence is often obtained for only a short period of time. Our findings suggest that the use of the vacuum method is desirable and recommended for single star simulations.

To further investigate the performance of the new vacuum method we have presented time evolutions of irrotational equal-mass binary neutron star configuration. Mainly, the merger and the postmerger dynamics are of great interest because the artificial atmosphere setup hinders the accurate computation of the ejecta [35]. Our analysis suggests that the ejecta materials are better conserved with the vacuum method. Around the moment of merger, the ejected mass, the ejecta velocity, and the kinetic energy of the ejecta are within the same range for both methods (vacuum and atmosphere) for all resolutions. But the difference in those quantities becomes prominent as the ejecta expands to larger radii, and the density of the ejecta drops below the atmosphere threshold. In the atmosphere cases this leads to ejecta removal and does not allow a free expansion of the ejecta material. In contrast, ejected matter can expand freely for the vacuum method.

ACKNOWLEDGMENTS

It is a pleasure to thank S. Bernuzzi and S. V. Chaurasia for fruitful discussions during this project. W. T. was supported by the National Science Foundation under Grants No. PHY-1305387 and No. PHY-1707227. B. B. was supported by DFG Grant No. BR-2176/5-1. Computations were performed on SuperMUC at the LRZ (Munich, Germany) under Projects No. pr46pu and No. pn56zo, Jureca (Jülich, Germany) under Project No. HPO21, and Stampede (Texas, XSEDE Allocation No. TG-PHY140019).

[1] E. Annala, T. Gorda, A. Kurkela, and A. Vuorinen, Phys. Rev. Lett. **120**, 172703 (2018).
[2] B. P. Abbott *et al.* (Virgo and LIGO Scientific Collaborations), Phys. Rev. Lett. **121**, 161101 (2018).
[3] S. De, D. Finstad, J. M. Lattimer, D. A. Brown, E. Berger, and C. M. Biwer, Phys. Rev. Lett. **121**, 091102 (2018).
[4] E. R. Most, L. R. Weih, L. Rezzolla, and J. Schaffner-Bielich, Phys. Rev. Lett. **120**, 261103 (2018).
[5] M. W. Coughlin, T. Dietrich, B. Margalit, and B. D. Metzger, Mon. Not. R. Astron. Soc. Lett. **489**, L91 (2019).
[6] C. D. Capano, I. Tews, S. M. Brown, B. Margalit, S. De, S. Kumar, D. A. Brown, B. Krishnan, and S. Reddy, Nat. Astron. **4**, 625 (2020).
[7] D. Radice and L. Dai, Eur. Phys. J. A **55**, 50 (2019).
[8] R. Essick, I. Tews, P. Landry, S. Reddy, and D. E. Holz, arXiv:2004.07744 [Phys. Rev. C (to be published)].
[9] T. Dietrich, M. W. Coughlin, P. T. Pang, M. Bulla, J. Heinzel, L. Issa, I. Tews, and S. Antier, arXiv:2002.11355.
[10] B. F. Schutz, Nature (London) **323**, 310 (1986).
[11] B. P. Abbott *et al.* (LIGO Scientific, VINROUGE, Las Cumbres Observatory, DLT40, Virgo, 1M2H, and MASTER Collaborations), Nature (London) **551**, 85 (2017).
[12] M. W. Coughlin, T. Dietrich, J. Heinzel, N. Khetan, S. Antier, M. Bulla, N. Christensen, D. A. Coulter, and R. J. Foley, Phys. Rev. Research **2**, 022006 (2020).
[13] S. Dhawan, M. Bulla, A. Goobar, A. S. Carracedo, and C. N. Setzer, Astrophys. J. **888**, 67 (2020).
[14] M. W. Coughlin, S. Antier, T. Dietrich, R. J. Foley, J. Heinzel, M. Bulla, N. Christensen, D. A. Coulter, L. Issa, and N. Khetan, Nat. Commun. **11**, 4129 (2020).
[15] P. S. Cowperthwaite *et al.*, Astrophys. J. **848**, L17 (2017).
[16] S. J. Smartt *et al.*, Nature (London) **551**, 75 (2017).
[17] M. M. Kasliwal *et al.*, Science **358**, 1559 (2017).
[18] D. Kasen, B. Metzger, J. Barnes, E. Quataert, and E. Ramirez-Ruiz, Nature (London) **551**, 80 (2017).
[19] D. Watson *et al.*, Nature (London) **574**, 497 (2019).
[20] B. P. Abbott *et al.* (LIGO Scientific, Virgo, Fermi GBM, INTEGRAL, IceCube, AstroSat Cadmium Zinc Telluride Imager Team, IPN, Insight-Hxmt, ANTARES, Swift, AGILE Team, 1M2H Team, Dark Energy Camera GW-EM, DES, DLT40, GRAWITA, Fermi-LAT, ATCA, ASKAP, Las Cumbres Observatory Group, OzGrav, DWF (Deeper Wider Faster Program), AST3, CAASTRO, VINROUGE, MASTER, J-GEM, GROWTH, JAGWAR, CaltechNRAO, TTU-NRAO, NuSTAR, Pan-STARRS,

MAXI Team, TZAC Consortium, KU, Nordic Optical Telescope, ePESSTO, GROND, Texas Tech University, SALT Group, TOROS, BOOTES, MWA, CALET, IKI-GW Follow-up, HESS, LOFAR, LWA, HAWC, Pierre Auger, ALMA, Euro VLBI Team, Pi of Sky, Chandra Team at McGill University, DFN, ATLAS Telescopes, High Time Resolution Universe Survey, RIMAS, RATIR, and SKA South Africa/MeerKAT Collaborations), Astrophys. J. **848**, L12 (2017).

[21] J. M. Ezquiaga and M. Zumalacárregui, Phys. Rev. Lett. **119**, 251304 (2017).

[22] T. Baker, E. Bellini, P. G. Ferreira, M. Lagos, J. Noller, and I. Sawicki, Phys. Rev. Lett. **119**, 251301 (2017).

[23] P. Creminelli and F. Vernizzi, Phys. Rev. Lett. **119**, 251302 (2017).

[24] M. Alcubierre, *Introduction to 3+1 Numerical Relativity* (Oxford University Press, New York, 2008).

[25] T. W. Baumgarte and S. L. Shapiro, *Numerical Relativity, Solving Einstein's Equations on the Computer* (Cambridge University Press, New York, 2010).

[26] L. Rezzolla and O. Zanotti, *Relativistic Hydrodynamics* (Oxford University Press, New York, 2013).

[27] B. P. Abbott *et al.* (LIGO Scientific and Virgo Collaborations), Phys. Rev. Lett. **119**, 161101 (2017).

[28] B. P. Abbott *et al.* (LIGO Scientific, Virgo, Fermi-GBM, and INTEGRAL Collaborations), Astrophys. J. **848**, L13 (2017).

[29] T. Yamamoto, M. Shibata, and K. Taniguchi, Phys. Rev. D **78**, 064054 (2008).

[30] M. Thierfelder, S. Bernuzzi, and B. Brügmann, Phys. Rev. D **84**, 044012 (2011).

[31] L. Baiotti and L. Rezzolla, Rep. Prog. Phys. **80**, 096901 (2017).

[32] D. Radice, L. Rezzolla, and F. Galeazzi, Classical Quantum Gravity **31**, 075012 (2014).

[33] J. R. Westernacher-Schneider, C. Markakis, and B. J. Tsao, Classical Quantum Gravity **37**, 155005 (2020).

[34] B. Brügmann, J. González, M. Hannam, S. Husa, U. Sperhake, and W. Tichy, Phys. Rev. D **77**, 024027 (2008).

[35] T. Dietrich, S. Bernuzzi, M. Ujevic, and B. Brügmann, Phys. Rev. D **91**, 124041 (2015).

[36] S. Bernuzzi and T. Dietrich, Phys. Rev. D **94**, 064062 (2016).

[37] T. Dietrich, S. Ossokine, and K. Clough, Classical Quantum Gravity **36**, 025002 (2019).

[38] Z.-j. Cao, H.-J. Yo, and J.-P. Yu, Phys. Rev. D **78**, 124011 (2008).

[39] B. Brügmann, W. Tichy, and N. Jansen, Phys. Rev. Lett. **92**, 211101 (2004).

[40] D. Pollney, C. Reisswig, E. Schnetter, N. Dorband, and P. Diener, Phys. Rev. D **83**, 044045 (2011).

[41] J. Thornburg, in *The Ninth Marcel Grossman Meeting: On Recent Developments in Theoretical and Experimental General Relavtivity, Gravitation, and Relativistic Field Theories*, edited by V. G. Gurzadyan, R. T. Jantzen, and R. Ruffini (World Scientific, Singapore, 2003), pp. 1743–1744.

[42] J. Thornburg, Classical Quantum Gravity **21**, 3665 (2004).

[43] M. Ruiz, D. Hilditch, and S. Bernuzzi, Phys. Rev. D **83**, 024025 (2011).

[44] D. Hilditch, S. Bernuzzi, M. Thierfelder, Z. Cao, W. Tichy, W. Tichy, and B. Brügmann, Phys. Rev. D **88**, 084057 (2013).

[45] S. Bernuzzi and D. Hilditch, Phys. Rev. D **81**, 084003 (2010).

[46] C. Bona, J. Massó, E. Seidel, and J. Stela, Phys. Rev. Lett. **75**, 600 (1995).

[47] M. Alcubierre, B. Brügmann, P. Diener, M. Koppitz, D. Pollney, E. Seidel, and R. Takahashi, Phys. Rev. D **67**, 084023 (2003).

[48] J. R. van Meter, J. G. Baker, M. Koppitz, and D.-I. Choi, Phys. Rev. D **73**, 124011 (2006).

[49] A. Sommerfeld, *Partial Differential Equation in Physics* (Academic Press, New York, 1949).

[50] F. Banyuls, J. A. Font, J. M. Ibáñez, J. M. Martí, and J. A. Miralles, Astrophys. J. **476**, 221 (1997).

[51] E. Chabanat, J. Meyer, P. Bonche, R. Schaeffer, and P. Haensel, Nucl. Phys. **A627**, 710 (1997).

[52] F. Douchin and P. Haensel, Astron. Astrophys. **380**, 151 (2001).

[53] J. S. Read, B. D. Lackey, B. J. Owen, and J. L. Friedman, Phys. Rev. D **79**, 124032 (2009).

[54] M. Shibata, K. Taniguchi, and K. Uryu, Phys. Rev. D **71**, 084021 (2005).

[55] A. Bauswein, H.-T. Janka, and R. Oechslin, Phys. Rev. D **82**, 084043 (2010).

[56] J. A. Font, M. Miller, W. M. Suen, and M. Tobias, Phys. Rev. D **61**, 044011 (2000).

[57] H. Dimmelmeier, J. A. Font, and E. Müller, Astron. Astrophys. **388**, 917 (2002).

[58] L. Baiotti, I. Hawke, P. J. Montero, F. Löffler, L. Rezzolla, N. Stergioulas, J. A. Font, and E. Seidel, Phys. Rev. D **71**, 024035 (2005).

[59] R. Borges, M. Carmona, B. Costa, and W. S. Don, J. Comput. Phys. **227**, 3191 (2008).

[60] C. Bona, J. Massó, and J. Stela, Phys. Rev. D **51**, 1639 (1995).

[61] M. Hannam, S. Husa, F. Ohme, B. Brügmann, and N. O'Murchadha, Phys. Rev. D **78**, 064020 (2008).

[62] T. Dietrich and B. Brügmann, J. Phys. Conf. Ser. **490**, 012155 (2014).

[63] M. Thierfelder, S. Bernuzzi, D. Hilditch, B. Brügmann, and L. Rezzolla, Phys. Rev. D **83**, 064022 (2011).

[64] A. Kurganov and E. Tadmor, J. Comput. Phys. **160**, 214 (2000), https://home.cscamm.umd.edu/people/faculty/tadmor/pub/central-schemes/Kurganov-Tadmor.JCP-00I.pdf.

[65] A. Lucas-Serrano, J. A. Font, J. M. Ibanez, and J. M. Marti, Astron. Astrophys. **428**, 703 (2004).

[66] H. Nessyahu and E. Tadmor, J. Comput. Phys. **87**, 408 (1990).

[67] J. A. Font, T. Goodale, S. Iyer, M. Miller, L. Rezzolla, E. Seidel, N. Stergioulas, W.-M. Suen, and M. Tobias, Phys. Rev. D **65**, 084024 (2002).

[68] M. J. Berger and P. Colella, J. Comput. Phys. **82**, 64 (1989).

[69] B. Giacomazzo and R. Perna, Astrophys. J. **758**, L8 (2012).

[70] C. Reisswig, R. Haas, C. D. Ott, E. Abdikamalov, P. Mösta, D. Pollney, and E. Schnetter, Phys. Rev. D **87**, 064023 (2013).

[71] T. Dietrich and S. Bernuzzi, Phys. Rev. D **91**, 044039 (2015).
[72] W. Tichy, Phys. Rev. D **74**, 084005 (2006).
[73] W. Tichy, Classical Quantum Gravity **26**, 175018 (2009).
[74] T. Dietrich, N. Moldenhauer, N. K. Johnson-McDaniel, S. Bernuzzi, C. M. Markakis, B. Brügmann, and W. Tichy, Phys. Rev. D **92**, 124007 (2015).
[75] A. Savitzky and M. J. E. Golay, Anal. Chem. **36**, 1627 (1964).
[76] A. Savitzky, Anal. Chem. **61**, 921A (1989).
[77] N. Stergioulas, A. Bauswein, K. Zagkouris, and H.-T. Janka, Mon. Not. R. Astron. Soc. **418**, 427 (2011).
[78] L. Rezzolla and K. Takami, Phys. Rev. D **93**, 124051 (2016).
[79] B. D. Metzger, Living Rev. Relativity **20**, 3 (2017).